Astronomy & Astrophysics

Gas phase Elemental abundances in Molecular cloudS (GEMS)

VIII. Unlocking the CS chemistry: The CH + S → CS + H and C$_2$ + S → CS + C reactions

Carlos M. R. Rocha[1], Octavio Roncero[2], Niyazi Bulut[3], Piotr Zuchowski[4], David Navarro-Almaida[5],
Asunción Fuente[6], Valentine Wakelam[7], Jean-Christophe Loison[8], Evelyne Roueff[9], Javier R. Goicoechea[2],
Gisela Esplugues[6], Leire Beitia-Antero[6], Paola Caselli[10], Valerio Lattanzi[10], Jaime Pineda[10], Romane Le Gal[11,12],
Marina Rodríguez-Baras[6], and Pablo Riviere-Marichalar[6]

[1] Laboratory for Astrophysics, Leiden Observatory, Leiden University, PO Box 9513, 2300-RA, Leiden, The Netherlands
[2] Instituto de Física Fundamental (IFF-CSIC), C.S.I.C., Serrano 123, 28006 Madrid, Spain
e-mail: `octavio.roncero@csic.es`
[3] University of Firat, Department of Physics, 23169 Elazig, Turkey
[4] Institute of Physics, Faculty of Physics, Astronomy and Informatics, Nicolaus Copernicus University in Torun, Grudziadzka 5, 87-100 Torun, Poland
[5] Université Paris-Saclay, CEA, AIM, Département d'Astrophysique (DAp), 91191 Gif-sur-Yvette, France
[6] Observatorio Astronómico Nacional (IGN), c/ Alfonso XII 3, 28014 Madrid, Spain
[7] Laboratoire d'astrophysique de Bordeaux, Univ. Bordeaux, CNRS, B18N, allée Geoffroy Saint-Hilaire, 33615 Pessac, France
[8] Institut des Sciences Moléculaires (ISM), CNRS, Univ. Bordeaux, 351 cours de la Libération, 33400 Talence, France
[9] Sorbonne Université, Observatoire de Paris, Univerité PSL, CNRS, LERMA, 92190 Meudon, France
[10] Centre for Astrochemical Studies, Max-Planck-Institute for Extraterrestrial Physics, Giessenbachstrasse 1, 85748 Garching, Germany
[11] Institut de Planétologie et d'Astrophysique de Grenoble (IPAG), Université Grenoble Alpes, CNRS, 38000 Grenoble, France
[12] Institut de Radioastronomie Millimétrique (IRAM), 300 Rue de la Piscine, 38406 Saint-Martin-d'Hères, France

ABSTRACT

Context. Carbon monosulphide (CS) is among the few sulphur-bearing species that have been widely observed in all environments, including in the most extreme, such as diffuse clouds. Moreover, CS has been widely used as a tracer of the gas density in the interstellar medium in our Galaxy and external galaxies. Therefore, a complete understanding of its chemistry in all environments is of paramount importance for the study of interstellar matter.

Aims. Our group is revising the rates of the main formation and destruction mechanisms of CS. In particular, we focus on those involving open-shell species for which the classical capture model might not be sufficiently accurate. In this paper, we revise the rates of reactions CH + S → CS + H and C$_2$ + S → CS + C. These reactions are important CS formation routes in some environments such as dark and diffuse warm gas.

Methods. We performed ab initio calculations to characterize the main features of all the electronic states correlating to the open shell reactants. For CH+S, we calculated the full potential energy surfaces (PESs) for the lowest doublet states and the reaction rate constant with a quasi-classical method. For C$_2$+S, the reaction can only take place through the three lower triplet states, which all present deep insertion wells. A detailed study of the long-range interactions for these triplet states allowed us to apply a statistic adiabatic method to determine the rate constants.

Results. Our detailed theoretical study of the CH + S → CS + H reaction shows that its rate is nearly independent of the temperature in a range of 10−500 K, with an almost constant value of 5.5×10^{-11} cm^3 s^{-1} at temperatures above 100 K. This is a factor of about 2−3 lower than the value obtained with the capture model. The rate of the reaction C$_2$ + S → CS + C does depend on the temperature, and takes values close to 2.0×10^{-10} cm^3 s^{-1} at low temperatures, which increase to $\sim 5.0 \times 10^{-10}$ cm^3 s^{-1} for temperatures higher than 200 K. In this case, our detailed modeling – taking into account the electronic and spin states – provides a rate that is higher than the one currently used by factor of approximately 2.

Conclusions. These reactions were selected based on their inclusion of open-shell species with many degenerate electronic states, and, unexpectedly, the results obtained in the present detailed calculations provide values that differ by a factor of about 2−3 from the simpler classical capture method. We updated the sulphur network with these new rates and compare our results in the prototypical case of TMC1 (CP). We find a reasonable agreement between model predictions and observations with a sulphur depletion factor of 20 relative to the sulphur cosmic abundance. However, it is not possible to fit the abundances of all sulphur-bearing molecules better than a factor of 10 at the same chemical time.

Key words. molecular processes – ISM: abundances – ISM: clouds – ISM: molecules

1. Introduction

Astrochemistry has become a necessary tool for understanding the interstellar medium (ISM) of our Galaxy and external galaxies. Nowadays, we are aware of the existence of nearly 300 molecules in the interstellar and circumstellar medium, as well as of around 70 molecules in external galaxies (for a complete list, see the Cologne Database for Molecular Spectroscopy[1]). Although the sulphur cosmic elemental abundance is only ten times lower than that of carbon (S/H $\approx 1.5 \times 10^{-5}$), only 33 out of the currently detected interstellar molecules contain sulphur atoms. This apparent lack of chemical diversity in astrophysical sulphur-bearing molecules is the consequence of a greater problem in astrochemistry: there is an unexpected paucity of sulphur-bearing species in dense molecular clouds and star-forming regions. In such dense regions, the sum of the observed gas-phase abundances of sulphur-bearing species (the most abundant are SO, SO_2, H_2S, CS, HCS^+, H_2CS, C_2S, C_3S, and NS) constitutes only <1% of the expected amount (Agúndez & Wakelam 2013; Vastel et al. 2018; Rivière-Marichalar et al. 2019; Hily-Blant et al. 2022) . One might postulate that most of the sulphur is locked on the icy grain mantles, but a similar trend is encountered within the solid phase, where s-OCS (the prefix "s-" indicates that the molecule is in the solid phase) and s-SO_2 are the only sulphur-bearing species detected so far (Palumbo et al. 1995, 1997; Boogert et al. 1997; Ferrante et al. 2008), and only upper limits to the s-H_2S abundance have been derived (Jiménez-Escobar & Muñoz Caro 2011). Recent observations with the *James Webb* Space Telescope (JWST) did not detect s-H_2S either (McClure et al. 2023). According to these data, the abundances of the observed icy species account for <5% of the total expected sulphur abundance. This means that 94% of the sulphur is missing in our counting. It has been suggested that this missing sulphur may be locked in hitherto undetected reservoirs in gas and icy grain mantles, or as refractory material (Shingledecker et al. 2020). In particular, laboratory experiments and theoretical work shows that sulphur allotropes, such as S_8, could be an important refractory reservoir (Jiménez-Escobar et al. 2014; Shingledecker et al. 2020; Cazaux et al. 2022).

Gas phase Elemental abundances in Molecular CloudS (GEMS) is an IRAM 30 m Large Program designed to estimate the S, C, N, and O depletions and the gas ionization fraction as a function of visual extinction in a selected set of prototypical star-forming filaments in low-mass (Taurus), intermediate-mass (Perseus), and high-mass (Orion) star forming regions (Fuente et al. 2019, 2023; Navarro-Almaida et al. 2020; Bulut et al. 2021; Rodríguez-Baras et al. 2021; Esplugues et al. 2022; Spezzano et al. 2022). Determining sulphur depletion is probably the most challenging goal of this project. The direct observation of the potential main sulphur reservoirs (s-H_2S, s-OCS, gas-phase atomic S) remains difficult even in the JWST era. Therefore, the sulphur elemental abundance needs to be estimated by comparing the observed abundances of rarer species, such as CS, SO, HCS^+, H_2S, SO_2, and H_2CS, with the predictions of complex gas-grain chemical models. In summary, the above factors mean that the sulphur chemistry in cold dark clouds remains a puzzling problem. The development of accurate and complete sulphur chemical networks is therefore required in order to disentangle the sulphur elemental abundance. Within the context of the GEMS project, we carried out a large theoretical effort to improve the accuracy of key reaction rates of the sulphur

chemical network, paying special attention to those associated with the formation and destruction paths of SO and CS, which are the gas-phase sulphur-bearing species observed in more different environments. We estimated the rates of the reactions S + O_2 → SO + O (Fuente et al. 2016) and SO + OH → SO_2 + H (Fuente et al. 2019) at the low temperatures prevailing in dark clouds. These reactions drive the SO chemistry in these cold environments. Bulut et al. (2021) estimated the rate constant of the CS + O → SO + O reaction, which has been proposed as an efficient CS destruction mechanism in molecular clouds. In the present work, we study two formation reactions of CS, which are thought to be important in regions with a low ionization fraction: CH($^2\Pi$) + S(^{3}P) and C_2($^1\Sigma_g^+$) + S(^{3}P). In both cases, the two reactants are radicals presenting several degenerate or quasi-degenerate electronic states: for CH + S, there are 36 degenerate states and for C_2 + S, the first excited C_2($^3\Pi_u$) states are only 0.089 eV above the C_2($^1\Sigma_g^+$) ground state. This makes the experimental determination of their rates difficult, because of the low densities in which two radical species are obtained, and because of the possibility of self-reactions. Therefore, the most accurate theoretical determination of the reaction rate constants is desirable in order to place satisfactory constraints on the abundance of CS in chemical models.

The reactions rates currently available for these two reactions were obtained with a classical capture method (Vidal et al. 2017). Dealing with open-shell systems, there are several degenerate electronic states for the reactants, not all of them leading to the desired product, and the crossing among them leads to barriers. All these effects are ignored in the classical capture method. Precise calculations like the ones in this article are needed to improve the accuracy of our chemical networks and to estimate the uncertainties associated with the less demanding classical capture methods.

2. CH+S reaction

The reaction

$$CH(^2\Pi) + S(^3P) \rightarrow CS(X^1\Sigma^+, a^3\Pi) + H \qquad (a)$$

$$\rightarrow SH(X^2\Pi) + C(^3P) \qquad (b)$$

$$(1)$$
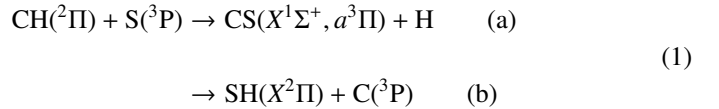
presents several rearrangement channels (CS and SH products) with several electronic states in each case. There are 36 degenerate states (neglecting spin-orbit couplings) in the CH($^2\Pi$) + S(^3P) entrance channel. There are the same number of degenerate states in the SH($X^2\Pi$) + C(^3P) rearrangement channel, which is only ≈0.08 eV below CH($^2\Pi$) + S(^3P). The reaction SH($X^2\Pi$) + C(^3P) → CS($X^1\Sigma^+, a^3\Pi$) + H has already been studied theoretically for the ground $^2A'$ state (Stoecklin et al. 1988, 1990a,b; Voronin 2004; Song et al. 2016) and for the excited $^2A''$ state (Zhang et al. 2018).

The 36 degenerate electronic states (neglecting spin-orbit couplings) involved in Eq. (1a) consist of 6 spin states times 6 orbital states. The spin states are quartet and doublets, while the orbital states are split into A' and A'' states, that is, symmetric or antisymmetric with respect to the inversion through the plane of the molecule. Of all these 36 states, only one doublet (i.e. 2 states) correlates to the CS($X^1\Sigma^+$) states, which correspond to the ground adiabatic $^2A'$ states. Reaction (1a) toward the $X^1\Sigma^+$ is exothermic by ≈3.5 eV. However, the excited CS($a^3\Pi$) is about 3.42 eV above CS($X^1\Sigma^+$), and the reaction is nearly thermoneutral.

2.1. Ab initio calculations

Here, to describe the electronic correlation along the reaction, we use the internally contracted multi-reference configuration interaction (ic-MRCI) method (Werner & Knowles 1988a,b), including the Davidson correction (hereafter referred to as MRCI+Q; Davidson 1975) and the calculations are performed with the MOLPRO suite of programs (Werner et al. 2012). Three electronic states are calculated for each symmetry, $3\,^2A'$ and $3\,^2A''$, and the same is true for the quartet states.

In these calculations, the molecular orbitals are optimized using a state-averaged complete active space self-consistent field (SA-CASSCF) method, with an active space of ten orbitals (seven a' symmetry and three a'' symmetry). Five $^{2,4}A'$ and four $^{2,4}A''$ electronic states are calculated and simultaneously optimized at CASSCF level using a dynamical weighting factor of 10. In all these calculations, the aug-cc-pVTZ (aVTZ) basis set is used (Dunning 1989). For the ic-MRCI calculations, six orbitals are kept doubly occupied, giving rise to $\approx 5 \times 10^6$ (382×10^6) contracted (uncontracted) configurations. Checks made with the aug-cc-pVQZ basis gave nearly parallel results along some of the minimum energy paths (MEPs) shown below. For this reason, we kept the aVTZ basis set to build the PES. Nevertheless, to better describe the long-range part, we use a AV5Z basis, as discussed below.

Figure 1 shows the first five A' and four A'' states for doublet (bottom) and quartet (top) multiplicities calculated at CASSCF level. With no spin-orbit couplings, the six electronic states for each multiplicity are degenerate for long distances of between $S(^3P)$ and $CH(X^2\Pi)$, and this asymptote is taken as the origin of energy. When they approach one another, they cross with the excited states correlating to $S(^3P) + CH(a^4\Sigma^-)$. After the crossing, there are three (two) curves for the doublet (quartet) states that become negative. For the doublets, one of these states correlates to $CS(X^1\Sigma^+)$ and two correlate to $CS(a^3\Pi_r)$ states.

This degeneracy is recovered in the MRCI+Q calculations shown in Fig. 2. The two degenerate states, $1^2A'$ and $1^2A''$ (and $1^4A'$ and $1^4A''$ for quartets), correspond to the $HCS(^2\Pi)$ radical (and the excited $HCS(^4\Pi)$) state, which experience Renner-Teller effects, as studied by Senekowitsch et al. (1990). In the case of doublets, the X^2A' state (of $^2\Pi$ character at collinear geometry) crosses with $2^2A'$ (of $^2\Sigma$ character at collinear geometry), which correlate with the $CS(X^1\Sigma^+)$ state of the products.

The crossing at collinear geometry is a conical intersection between Σ and Π states. As long as the system bends, there are couplings and the crossing is avoided. As a consequence, the ground X^2A' state correlates to the $CS(X^1\Sigma^+)$ products, that is, only these two doublets among the 36 states correlating to the $CH(^2\Pi)+S(^3P)$ reactants. Therefore, only the ground electronic state is needed to describe the reaction (1). The energy difference between the $CH(^2\Pi)+S(^3P)$ and $CS(X^1\Sigma^+) + H$ at their corresponding equilibrium geometries is $D_e = 3.52$ eV, and $D_0 = 3.62$ eV when including zero-point energy (using the fit described below). As there have been no direct measurements for this reaction, the experimental exothermicity is estimated from the dissociation energies $D_0 = D_0^{CH} - D_0^{CS} = 3.89$ eV, using the values reported by Huber & Herzberg (1979), and this D_0 is about 10% higher than the present results.

2.2. Long-range interaction

MRCI calculations are not size consistent and the Davidson correction (+Q) is not adequate to describe closely lying electronic states. Therefore, the MRCI+Q method introduces inaccuracies
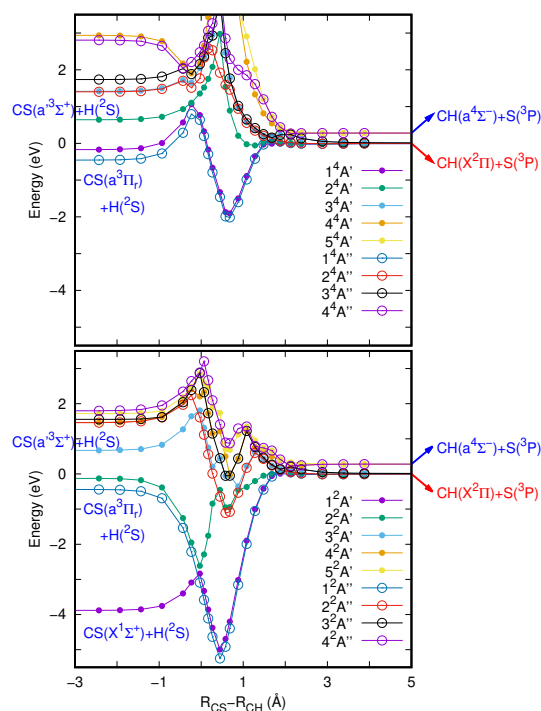

Fig. 1. CASSCF energies along the reaction coordinate defined as the R_{CS}-R_{CH} distance difference. The energies shown here are obtained for an angle $\gamma_{SCH} = 179.9°$ for the doublet (bottom panel) and quartet (top panel) states for the $CH + S \rightarrow CS + H$ reaction. Here, we consider five A' and four A'' electronic states.
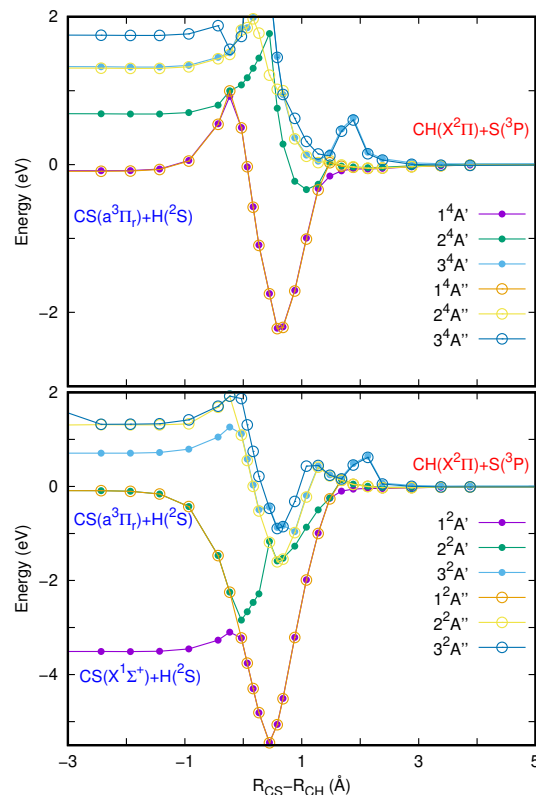

Fig. 2. MRCI+Q energies along the reaction coordinate defined as the $R_{CS}-R_{CH}$ distance difference. The energies shown here are obtained for an angle $\gamma_{SCH} = 179.9°$ for the doublet (bottom panel) and quartet (top panel) states, for the $CH + S \rightarrow CS + H$ reaction. Three A' and three A'' electronic states are considered in each case.
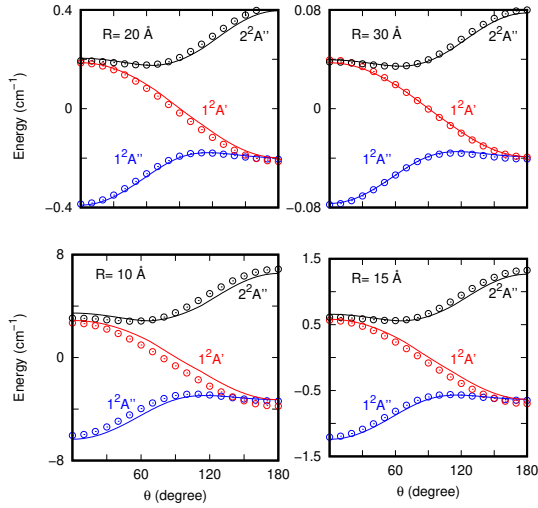
Fig. 3. Angular dependence of the long-range interaction between CH and S in the three lower electronic states. Points are the CASSCF(aV5Z) energies (in cm^{-1}) as a function of the Jacobi angle θ (defined in the text) for $r_{CH} = 1.1199$ Å and $R = 10, 15, 20$ and 30 Å, as indicated in each panel, for the $1^2A''$, $1^2A'$, and $2^2A''$ states. Lines correspond to the long-range analytical fit of Eq. (2) taken from Zeimen et al. (2003).

in the long-range region, which need to be described accurately in order to obtain good rate constants at low temperatures. Coupled cluster methods are size consistent and are typically considered to be the best way to describe long-range interactions; however, in the presence of two open shell reactants, even these methods are not expected to yield good accuracy.

Here, as an alternative, we use the CASSCF method with a larger aV5Z basis set (Dunning 1989). Several points have been calculated in Jacobi coordinates, for CH(r_{CH}) = 1.1199 Å and $R = 10$–50 Å, where R is the distance between the CH center of mass and the S atom as a function of the angle θ, with $\cos\theta = \mathbf{R} \cdot \mathbf{r}_{CH}/Rr_{CH}$. At long distances, the system behaves as a dipole-quadrupole interaction, with the dipole of CH interacting with the quadrupole of a P sulphur atom whose analytical form is (Zeimen et al. 2003)

$$V_{LR}(R,\theta) = M_{QD}(\theta)\frac{Q_A d_B}{R^4} + M_{QQ}(\theta)\frac{Q_A Q_B}{R^5}, \qquad (2)$$

with $M_{QD}(\theta)$ and $M_{QQ}(\theta)$ being 3×3 matrices, depending on Legendre polynomials (Zeimen et al. 2003). The eigenvalues of this matrix properly describe the angular dependence of the adiabatic states. Therefore, only two effective parameters are needed to fit the ab initio points, $Q_A d_B = 0.293$ hartree Å^{-4} and $Q_A Q_B = 0.092$ hartree Å^{-5}. Two families of three states are considered separately, namely $1^2A''$, $1^2A'$, $2^2A''$ and $2^2A'$, $3^2A'$, $3^2A''$, corresponding to the two Π states of CH interacting with the three P states of sulphur. The excellent agreement between calculated and fitted analytical expressions, as shown in Fig. 3, demonstrates the adequacy of the analytical fit in the asymptotic region.

2.3. Analytical fit of the ground state

The analytical representation of the potential energy surface of the ground $1^2A'$ electronic state is described by two terms

$$V(r_{CH}, r_{CS}, r_{SH}) = E_g^{FF}(r_{CH}, r_{CS}, r_{SH}) + V^{3B}(r_{CH}, r_{CS}, r_{SH}), \qquad (3)$$

where V^{3B} is the three-body term added to the zero-order description provided by the lowest root, $E_g^{FF}(r_{CH}, r_{CS}, r_{SH})$, of the

3×3 reactive force-field matrix defined as (Zanchet et al. 2018; Roncero et al. 2018; Goicoechea et al. 2021)

$$H^{FF} = \begin{pmatrix} V_{CH} + W_{CS}^1 + W_{SH}^1 + V_{LR} & V_{12} & V_{13} \\ V_{12} & V_{CS} + W_{CH}^2 + W_{SH}^2 & V_{23} \\ V_{13} & V_{23} & V_{SH} + W_{CH}^3 + W_{CS}^3 \end{pmatrix}. \qquad (4)$$

The diagonal terms describe each of the rearrangement channels, in which $V_{CH}(r_{CH})$, $V_{CS}(r_{CS})$, and $V_{SH}(r_{SH})$ are fitted using the diatomic terms of Aguado & Paniagua (1992). In the reactant channel 1, the long-range term given by Eq. (2) is included. W_{AB} are Morse potentials whose parameters are determined to describe each channel independently. Finally, the nondiagonal terms V_{ij} are built as Gaussian functions $\exp(-\alpha(H_{ii}^{FF} - H_{jj}^{FF})^2)$ depending on the energy difference between the diagonal terms of the corresponding force-field matrix. The parameter α is determined to fit the transition between rearrangements.

The three-body term V^{3B} in Eq. (3) is described with the method of Aguado & Paniagua (1992) using a modification of the program GFIT3C (Aguado et al. 1998). We included about 7500 ab initio points calculated at MRCI+Q level in the fit. These points are mainly composed of a grid of 22 points for $0.6 \le r_{CH} \le 8$ Å, 27 points for $1 \le r_{CS} \le 8$ Å, and 19 points in the θ_{HCS} angle, in intervals of $10°$. The points are weighted with a weight of 1 for those with energy up to 1 eV from the entrance CH+S channel at 50 Å, and with a Gaussian function for higher energies, considering a minimum weight of 10^{-4}. The final fit uses polynomials up to order 10, with an overall root-mean-square error of 0.07 eV.

The main features of the potential fit are shown in Fig. 4, where the contour plots for the reactants (bottom panel, for $R_{CH} = 1.1199$ Å) and products (top panel, for $R_{CS} = 1.568$ Å, and shifted by 3.526 eV, which is the exoergicity of the reaction) are shown. The CH+S reactant channel (bottom panel) is attractive for $R_{CS} < 7$ Å, leading to the products channel at $R_{CS} \approx 1.5$ Å, with an energy of –5.5 eV. These energies correspond to the CS-H well in the products channel, which is about 2 eV below the CS + H products shown in the top panel of Fig. 4, which have been shifted by 3.526 eV to show the details. At $R_{CH} \approx 2$ Å, there is a barrier that arises from the curve crossing discussed above.

2.4. Quasi-classical versus quantum wave packet dynamics in the $1^2A'$ state

To check the validity of the quasi-classical method, we first compare quantum and quasi-classical trajectory (QCT) calculations for total angular momentum $J = 0$. The quantum wave packet (WP) calculations are performed with the MADWAVE3 code (Zanchet et al. 2009) and the parameters used are listed in Table 1. The WP method is considered numerically exact but is very computationally demanding. The QCT calculations are performed with the MDwQT code (Sanz-Sanz et al. 2015; Zanchet et al. 2016; Ocaña et al. 2017). Initial conditions are sampled with the usual Monte Carlo method (Karplus et al. 1965). In this first set of calculations, CH is in its ground vibrational (v) and rotational state, $(v, j) = (0, 0)$, and the initial internuclear distance and velocity distributions are obtained with the adiabatic switching method (Grozdanov & Solov'ev 1982; Qu & Bowman 2016; Nagy & Lendvay 2017). We consider an impact parameter $b = 0$, which corresponds to $J = 0$. The initial distance between sulfur and the CH center of mass is set to 50 Bohr, and the trajectories are stopped when any internuclear distance is greater than 60 Bohr. For each energy, $N_{tot} = 10^4$ trajectories are run to
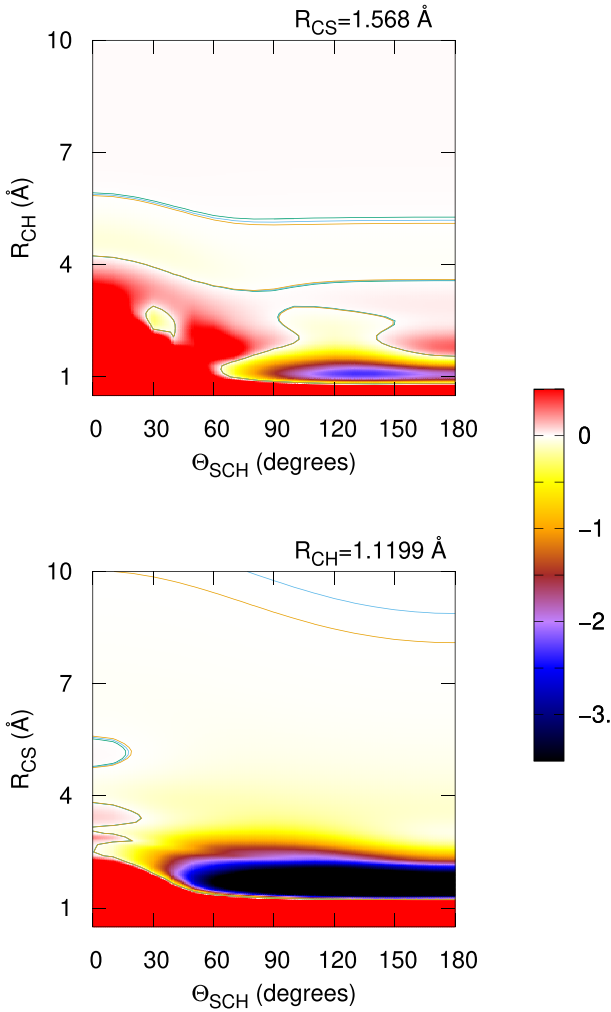
$R_{CS} = 1.568$ Å

$R_{CH} = 1.1199$ Å

Fig. 4. Contour plots of the analytical potential energy surfaces fitted to ab initio points, corresponding to the reactant channel for $R_{CH} = 1.1199$ Å (bottom panel) and to the products channel for $R_{CS} = 1.568$ Å (top panel). Energies are in eV. For the products, the energies are shifted by 3.526 eV, so that their point of zero energy corresponds to the $CS(r_{eq})$ at an infinite distance from H. The contours correspond to 0 and ± 1 meV in order to show the dependence of the potential at long distances. The units of the color box are eV.

calculate the reaction probability as $P_R(E) = N_r/N_{tot}$, where N_r is the number of reactive trajectories.

The WP and QCT reaction probabilities are compared in Fig. 5, and the results from the two methods show very similar behavior: a reaction probability slightly higher than 0.9 at energies below 0.01 eV, decreasing as a function of collision energy down to a probability of lower than 0.2 at 1 eV. In the two cases, there are oscillations, which do not match perfectly but show similar envelopes. As these oscillations are expected to wash out when considering the partial wave summation over total angular momentum, J, we consider this agreement to be satisfactory. This leads us to conclude that the QCT method is sufficiently accurate to determine the reaction rate constant, as described below.

The reaction rate constant for CH($v = 0$ and 1) in the $1^2A'$ electronic state is evaluated according to

$$K_v^{1^2A'}(T) = \sqrt{\frac{8k_B T}{\pi \mu}} \pi b_{max}^2(T) P_r(T), \qquad (5)$$

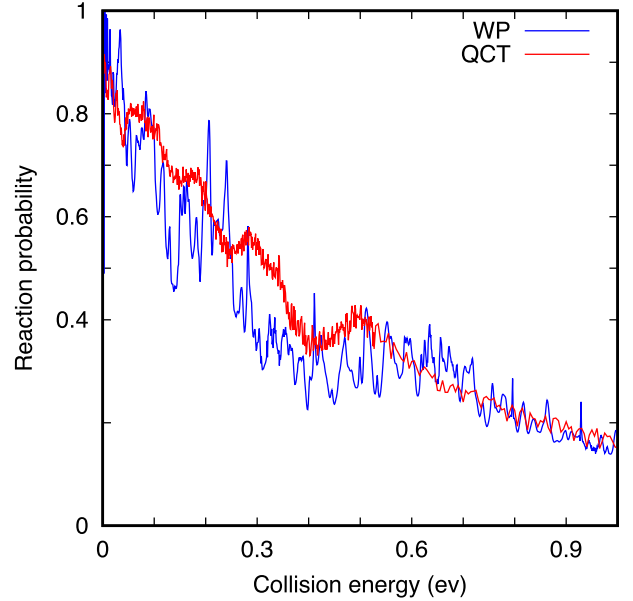**Fig. 5.** CH+S → CS + H reaction probabilities versus collision energy for $J = 0$ in the $1\,^2A'$ electronic state using quantum wave packet and quasi-classical trajectory methods.

Table 1. Parameters used in the wave packet calculations in reactant Jacobi coordinates.

$r_{min}, r_{max} = 0.1, 17$ Å	$N_r = 420$
$r_{abs} = 5$ Å	
$R_{min}, R_{max} = 0.001, 17.5$ Å	$N_R = 840$
$R_{abs} = 10.5$ Å	
$N_\gamma = 168$	in $[0, \pi]$
$R_0 = 10$ Å	$E_0, \Delta E = 0.35, 0.2$ eV
$r_\infty = 4$ Å	

Notes. $r_{min} \leq r \leq r_{max}$ is the CH internuclear distance, $R_{min} \leq R \leq R_{max}$ is the distance between the CH center of mass and the sulphur atom, and $0 \leq \gamma \leq \pi$ is the angle between r and R vectors. The initial wave packet is described in R by a Gaussian centered at $R = R_0$, and at a translational energy of $E = E_0$, and width ΔE. The total reaction probability is obtained by analyzing the total flux at $r = r_\infty$.

where $b_{max}(T)$ and $P_r(T)$ are the maximum impact parameter and reaction probability at constant temperature, respectively. In this case, about 10^5 trajectories are run for each temperature, which is also true for translation and rotation degrees of freedom, fixing the vibrational state of CH to $v = 0$ or 1.

2.5. Thermal rate

Considering that only the double degenerate $1^2A'$ electronic state reacts to form $CS(X^1\Sigma^+)$, the electronic partition function has to be considered. Neglecting the spin-orbit splitting, the electronic partition function would be 2/36, that is, the thermal rate constant is about 1/18 of the reaction rate, $K^{1^2A'}$, associated to the $1^2A'$ state. Including the spin-orbit splitting of the $S(^3P_{J_s})$ sulphur atom, and assuming that only the lowest two spin-orbit states react (having an individual rate constant equal to $K^{1^2A'}$),
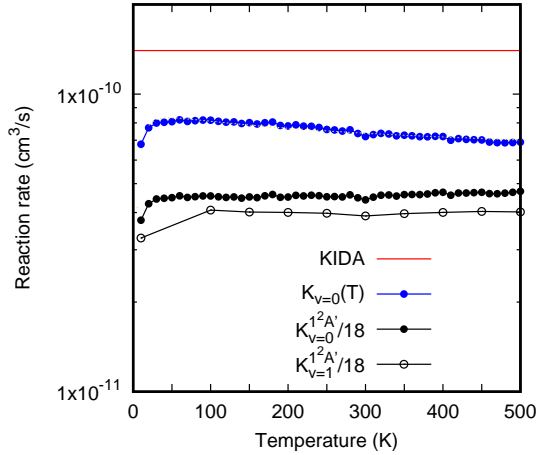
Fig. 6. Vibrational-selected rate constant for the CH($X^2\Pi$,v = 0) + S(^3P) $\rightarrow$ CS($X^1\Sigma$) + H reaction, obtained here according to Eq. (6).

Table 2. Parameters used to fit the total reaction rates calculated for CH+S and C_2 + S, according to the expression $K(T) = A(T/300)^B e^{-C/T}$

Reaction	A (cm^3 s^{-1})	B	C (K)
CH + S	7.52×10^{-11}	–0.117	5.42
C_2 + S	5.08×10^{-10}	0.121	2.70

the vibrational selected thermal rate constant is given by

$$K_v(T) = \frac{2K_v^{1^2A'}(T)}{4\left[5 + 3\exp(-539.83/T) + \exp(-825.34/T)\right]}, \quad (6)$$

and is shown in Fig. 6. In this figure, the red line corresponds to the rate constant (1.4×10^{-10} cm^3 s^{-1}) obtained from the KIDA data base, as obtained with a classical capture model (Vidal et al. 2017), using analytical formulas (Georgievskii & Klippenstein 2005; Woon & Herbst 2009) with dipole moments and polarizabilities taken from the literature or calculated using density functional theory.

The $K_{v=0}^{1^2A'}(T)/18$ rate constant at 10 K is about 4×10^{-11} cm^3 s^{-1}, increasing to a nearly constant value of $\approx 5.5 \times 10^{-11}$ cm^3 s^{-1} at temperatures above 100 K. This is a factor of between 2 and 3 lower than the value obtained with the capture model (Vidal et al. 2017).

When including the spin-orbit splitting, the rate $K_{v=0}(T)$ is larger at 10 K, simply because the populations of the excited sulphur spin-orbit states, $J_S = 1$ and 0, are negligible. As temperature increases, their populations increase, leading to a reduction of the rate constant $K_{v=0}(T)$, which decreases tending to $K^{1^2A'}(T)/18$ at high temperature. The rate with spin-orbit splittings, $K_{v=0}(T)$, is only a factor $\approx 1/2$ smaller than that of KIDA at 10 K, and is considered the most accurate obtained here. The $K_{v=0}(T)$ rate constant has been fitted and the parameters are listed in Table 2.

We also show $K_{v=1}^{1^2A'}(T)/18$ in Fig. 6. Its contribution at low temperatures is small, because the vibration energy of CH(v = 1) is about 0.337 eV higher than $v = 0$, that is, 3916 K. Therefore, $K_{v=0}(T)$ is a good approximation of the thermal rate constant, which includes the spin–orbit splitting.
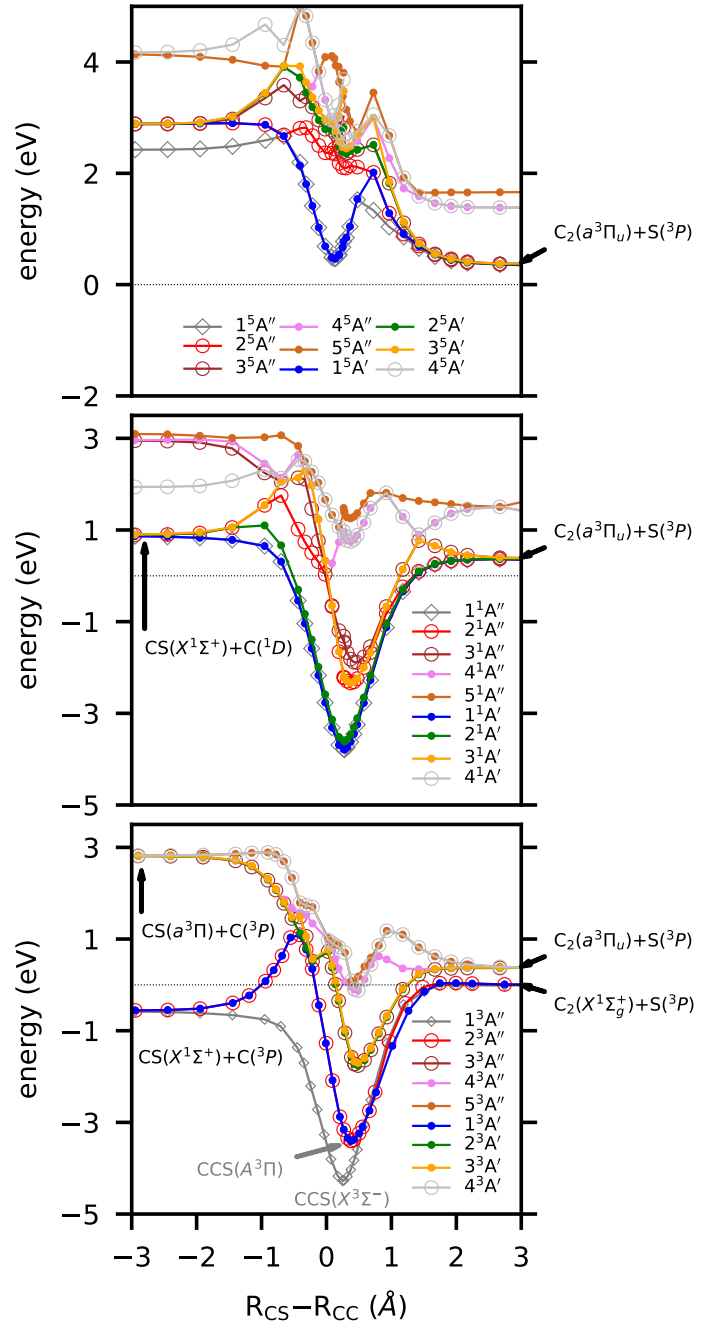
Fig. 7. CASSCF/aVTZ optimized reaction paths for the conversion between C_2+S and CS+C, which occurs on several potential energy surfaces of CCS. The reaction coordinate is defined as $R_{CS} - R_{CC}$, while the valence angle, γ_{CCS}, was held fixed at 179.9° in the geometry optimizations. Five A'' and four A' electronic states of CCS were considered for each multiplicity: triplet (bottom panel), singlet (middle panel), and quintet (top panel).

3. C_2+S reaction

The reaction

$$C_2(X^1\Sigma_g^+) + S(^3P) \rightarrow CS(X^1\Sigma^+) + C(^3P) \quad (7)$$
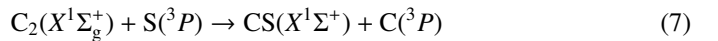
is exothermic by ~ 1 eV (Visser et al. 2019; Reddy et al. 2003). Due to the open-shell nature of the involved atoms [S(^3P) and C(^3P)], reactant collision and product formation can take place adiabatically on three triplet CCS potential energy surfaces ($2^3A''+1^3A'$); see, for example, Figs. 7 and 8. To the best of
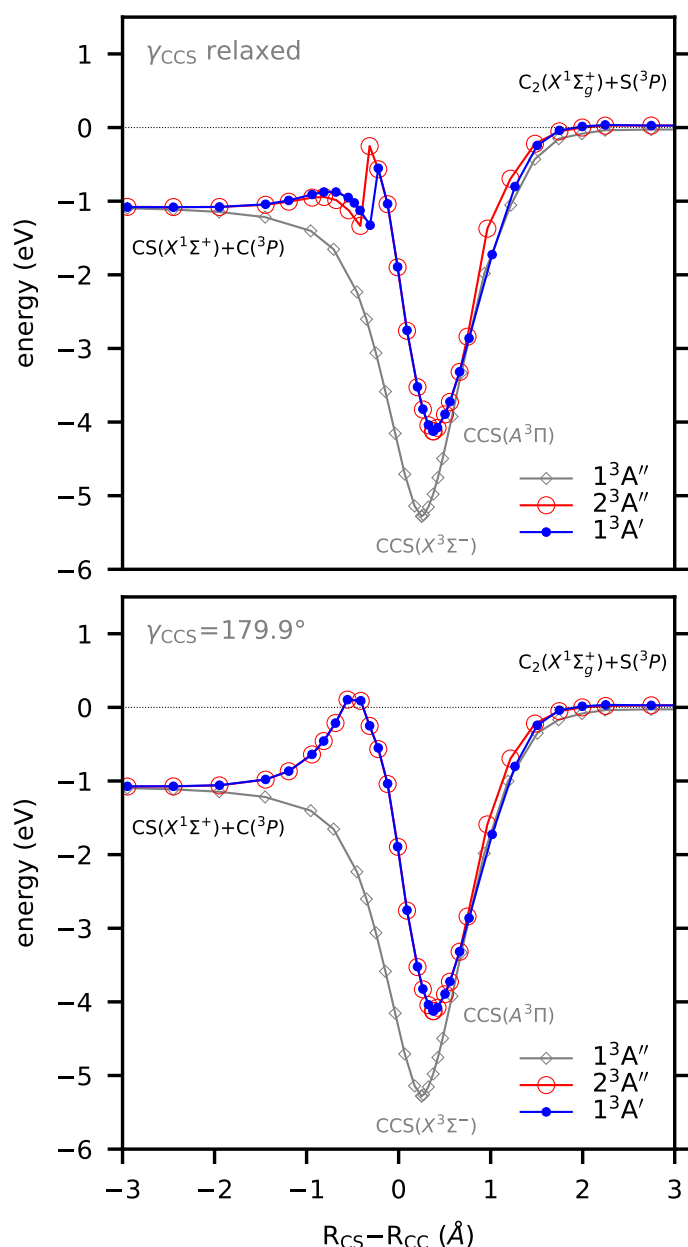
Fig. 8. Optimized reaction paths for $C_2(X^1\Sigma_g^+) + S(^3P) \rightarrow CS(X^1\Sigma^+) + C(^3P)$ as obtained from MRCI+Q/aVQZ//CASSCF/aVQZ calculations. The reaction coordinate is defined as $R_{CS} - R_{CC}$. In the bottom panel, the valence angle, γ_{CCS}, was held fixed at $179.9°$ in the geometry optimizations, while, in the top panel, it was freely optimized along with R_{CS} or R_{CC} bond distances. Two $^3A''$ and one $^3A'$ triplet electronic states of CCS were considered in each case.

our knowledge, there have been no theoretical studies dedicated to this reaction. Vidal et al. (2017) reported a theoretical upper limit for its rate coefficient ($k \sim 2 \times 10^{-10}$ cm^3 molecule^{-1} s^{-1} at 10 K) using classical capture rate theory. From an experimental viewpoint, presently available techniques for the production of reactant dicarbon often generate a mixture of both $C_2(X^1\Sigma_g^+)$ and $C_2(a^3\Pi_u)$ (Gu et al. 2006; Páramo et al. 2008). It is important to note that this electronically excited state lies only ~ 716 cm^{-1} above the ground X form, which – together with the expected high reactivity of C and S atoms – make the laboratory characterization of this specific reaction (7) extremely cumbersome.

3.1. Ab initio calculations

The methodology we employed to obtain optimized energy paths for the $C_2 + S \rightarrow CS + C$ reaction closely resembles that used for the CH + S system. Our preliminary PES explorations and geometry optimizations were all performed at the SA-CASSCF level of theory, followed by single-point MRCI+Q calculations. The CASSCF active space involves a total of 14 correlated electrons in 12 active orbitals ($9a' + 3a''$). For each multiplicity considered (triplet, singlet and quintet), we treated five A'' and four A' electronic states simultaneously in the SA-CASSCF wave functions. The aVXZ ($X = T, Q$) basis sets of Dunning and co-workers (Dubernet & Hutson 1994; Kendall et al. 1992) were employed throughout, with the calculations done with MOLPRO.

Our calculated CASSCF/aVTZ optimized path for reaction (7) is shown in the bottom panel of Fig. 7. As seen, the $C_2(X^1\Sigma_g^+) + S(^3P)$ reactant collision involves only triplet CCS PESs and can happen on two $^3A''$ and one $^3A'$ electronic states. Proceeding through the ground-state PES of CCS($1^3A''$), reaction (7) does not encounter any activation barriers for collinear atom-diatom approaches, being exothermic by ~ 0.6 eV at CASSCF/aVTZ level. We note that this process occurs via the formation of a strongly bound intermediate complex corresponding to the linear global minimum of CCS, ℓ-CCS($X^3\Sigma^-$) (Saito et al. 1987); from this structure, the ground-state CS($X^1\Sigma^+$) + C(^3P) products can be directly accessed, without an exit barrier.

A close look at Fig. 7 (bottom panel) also reveals that the excited $2^3A''$ and $1^3A'$ electronic states are degenerate along $C_{\infty v}$ atom-diatom collisions. These PESs form the Renner-Teller components of the strongly bound ℓ-CCS($A^3\Pi$) complex, showing a conical intersection with ℓ-CCS($X^3\Sigma^-$) at $R_{CS} - R_{CC} \approx +0.5$ Å (Riaplov et al. 2003; Tarroni et al. 2007). As opposed to the ground $1^3A''$ state, the conversion from reactants to products as proceeding adiabatically through the $2^3A''$ and $1^3A'$ PESs entails a large activation barrier (≈ 1 eV at CASSCF/aVTZ level), which is located at $R_{CS} - R_{CC} \approx -0.5$ Å; see Fig. 7. As shown, this region of the nuclear configuration space is extremely congested by the existence of several low-lying excited triplet states correlating with $C_2(a^3\Pi_u) + S(^3P)$. We note that the $C_2(a^3\Pi_u) + S(^3P)$ reactants can approach each other in six triplet ($3^3A'' + 3^3A'$), six singlet ($3^1A'' + 3^1A'$), and six quintet ($3^5A'' + 3^5A'$) electronic states. For completeness, their corresponding optimized reaction paths toward CS+C formation are also plotted in Fig. 7; see bottom, middle, and top panels therein. Accordingly, when proceeding adiabatically, the reactions involving $C_2(a^3\Pi_u) + S(^3P)$ are all endothermic, ultimately leading to excited-state CS+C products. These are therefore are expected to be highly inefficient at the low temperature regimes envisaged here (unless nonadiabatic transitions play a role) and are not considered further in this work for this reason.

Maintaining our focus on the target $C_2(X^1\Sigma_g^+) + S(^3P) \rightarrow CS(X^1\Sigma^+) + C(^3P)$ process (reaction (7)) and to better estimate its overall attributes, we performed MRCI+Q/aVQZ//CASSCF/aVQZ calculations along the underlying reaction paths on $1^3A''$, $2^3A''$, and $1^3A'$ electronic states. The results are plotted in Fig. 8. Accordingly, at this level of theory, our best estimate for the exothermicity of reaction (7) is 1.05 eV (without zero-point energy), a value that almost perfectly matches the corresponding experimental estimate of 1.04 eV (Visser et al. 2019; Reddy et al. 2003). The stabilization energies of the ℓ-CCS($X^3\Sigma^-$) and ℓ-CCS($A^3\Pi$) complexes are herein predicted to be -5.3 and -4.2 eV, respectively, relative to the $C_2(X^1\Sigma_g^+) + S(^3P)$ reactant channel. Most notably, Fig. 8

(bottom panel) shows that, at MRCI+Q/aVQZ//CASSCF/aVQZ level, the predicted activation barriers along linear $C_{\infty v}$ paths for the $2^3A''$ and $1^3A'$ states are largely reduced with respect to CASSCF/aVTZ values (Fig. 7; bottom panel), going from ≈ 1 to less than 0.1 eV. Indeed, by allowing the valence C–C–S angle (γ_{CCS}) to also be freely optimized in the MRCI+Q/aVQZ//CASSCF/aVQZ calculations, Fig. 8 (top panel) unequivocally shows that such barriers actually become submerged, lying below the corresponding $C_2(X^1\Sigma_g^+) + S(^3P)$ reactant channel; we note the existence of small discontinuities on the ab initio curves that are associated with abrupt changes in γ_{CCS} near the top of these barriers. This clearly indicates that all such PESs ($1^3A''$, $2^3A''$, and $1^3A'$) contribute to the overall dynamics and kinetics of reaction (7), even at low temperatures. In the following, we describe the methodology employed to obtain rate coefficients for this target reaction.

3.2. Long-range interactions

Restricting the calculations to the equilibrium distance of $C_2(^1\Sigma_g^+)$ allows us to consider $C_2(^1\Sigma_g^+)$ and $C_2(^3\Pi)$ separately. Under this approximation, the situation simplifies to a closed shell diatom plus an open shell atom for the two asymptotes $C_2 + S$ and $CS + C$. For both cases, let us adopt the Jacobi coordinate system and expansion in terms of orthogonal functions as defined, for example, in Flower & Launay (1977); Dubernet & Hutson (1994):

$$V(R, \theta, \phi, \theta_a, \phi_a) = \sum_{\lambda\lambda_a\mu} V_{\lambda\lambda_a\mu}(R) C_{\lambda\mu}(\theta, \phi) C_{\lambda_a,-\mu}(\theta_a\phi_a), \quad (8)$$

where $C_{\lambda\mu}(\theta, \phi) = \left(\frac{4\pi}{2\lambda+1}\right)^{1/2} Y_{\lambda\mu}(\theta, \phi)$ are spherical harmonics in Racah normalization. The θ, ϕ angles correspond to the orientation of diatomic molecules with respect to the vector connecting the center of mass of the diatomic molecule with the atom in a Jacobi frame, while θ_a, ϕ_a angles correspond to the orientation of the doubly occupied p orbital of the S and C atom, respectively. The R is the distance between the center of mass of the diatom and the atom. For both systems in C_s symmetry, the solution of the electronic Schrödinger equation is hard, because single-reference methods cannot be used due to the fact that two solutions will always belong to the same irreducible representation, and are nearly degenerate. The situation is simpler in the case of symmetric configurations: $C_{\infty v}$ (linear) for both systems, and C_{2v} (T-shaped) for $C_2 + S$. For these cases, atom+diatom states belong to distinct irreducible representations: for linear geometry Π and Σ^- states, while for C_{2v} these symmetries are B_1, B_2, and A_2. For these particular configurations of the CCS system, the single-reference gold-standard CCSD(T) method can be used for calculations of interaction energy in each symmetry (Alexander 1998; Klos et al. 2004; Atahan et al. 2006).

Using linear and T-shape geometries, we calculated UCCSD(T) interaction energies in the range of 6–30 Å and converted them to $V_{\lambda\lambda_r\mu}(R)$ potentials using the following formula for C_2+S,

$$V_{000} = (2V_\Pi + V_\Sigma + 2V_{B_1} + 2V_{B_2} + 2V_{A_2})/9 \quad (9)$$
$$V_{020} = -2(V_\Pi - V_\Sigma + V_{B_1} + V_{B_2} - 2V_{A_2})/9 \quad (10)$$
$$V_{200} = 2(2V_\Pi + V_\Sigma - 2V_{B_1} - V_{B_2} - V_{A_2})/9 \quad (11)$$
$$V_{220} = -2(2V_\Pi - 2V_\Sigma - V_{B_1} - V_{B_2} + 2V_{A_2})/9, \quad (12)$$

and the following formula for CS+C,

$$V_{000} = (2V_{\Pi,0} + V_{\Sigma,0} + 2V_{\Pi,180} + V_{\Sigma,180})/6 \quad (13)$$

$$V_{100} = (2V_{\Pi,0} + V_{\Sigma,0} - (2V_{\Pi,180} + V_{\Sigma,180}))/6 \quad (14)$$
$$V_{020} = (V_{\Sigma,0} - V_{\Pi,0} + V_{\Sigma,180} - V_{\Pi,180})/3 \quad (15)$$
$$V_{120} = (V_{\Sigma,0} - V_{\Pi,0} - (V_{\Sigma,180} - V_{\Pi,180}))/3, \quad (16)$$

where, in the latter equation, $V_{\Pi,0}/V_{\Sigma,0}$ and $V_{\Pi,180}/V_{\Sigma,180}$ denote the potential for appropriate symmetry in the C–S–C and C–C–S configurations, respectively. The above equations can be obtained by calculating Eq. (8) for $\theta, \phi, \theta_a, \phi_a$, which correspond to symmetric configurations (Flower & Launay 1977).

The $V_{\lambda\lambda_r\mu}(R)$ potentials were then carefully fitted to an analytical form in order to obtain the inverse power expansion form. It is important to take into account that collision-induced rotations of CS molecules are driven directly by V_{100} and V_{120} terms, while for C_2 molecules colliding with atoms, the driving terms are V_{200} and V_{220}. When the atoms are assumed to be spherically symmetric, the terms V_{120} and V_{220} can be ignored. Therefore, hereafter we skip the dependence on θ_a, ϕ_a in Eq. (8). Thus, our model of the potential used for the statistical method includes only the isotropic term V_{000} and the leading anisotropies V_{100} and V_{200}, which were fitted to analytical forms of van der Waals expansion: $\sum_{i=0}^3 C_{6+i}R^{-(6+i)}$ for V_{000} and V_{200}, and $\sum_{i=0}^3 C_{7+i}R^{-(7+i)}$ for V_{100}. These potentials can be viewed as averaged over all orientations of P-state atoms. Moreover, for the leading coefficients, we also performed similar calculations using open-shell symmetry adapted perturbation theory (Hapka et al. 2012) and confirm the values for the leading coefficients C_6 and C_7 of the reactants and products (these agree to within 10%).

The final analytical form of the potential used for $C_2 + S$ reads (in atomic units of distance and energy)

$$V(R, \theta) = A R^{-6} + B R^{-8} + C R^{-10} \quad (17)$$
$$+ \frac{1}{2}(3\cos^2(\theta) - 1)(D R^{-6} + E R^{-8} + F R^{-10}),$$

with $A = -125.8$, $B = -9.444 \times 10^3$, $C = 1.743 \times 10^5$, $D = -13.66$, $E = -2.848 \times 10^3$, and $F = -1.929 \times 10^5$, while for CS+C,

$$V(R, \theta) = A R^{-6} + B R^{-8} + C R^{-10} \quad (18)$$
$$+ D R^{-12} + \frac{\cos(\theta)}{R^{-7}}(E + F R^{-2} + G R^{-4} + H R^{-6}),$$

with $A = -147.5$, $B = -207.3$, $C = -3.834 \times 10^6$, $D = -2.805 \times 10^8$, $E = -487.3$, $F = -4.309 \times 10^3$, $G = -2.394 \times 10^7$, and $H = -1.997 \times 10^9$.

3.3. Rate constant calculations

Due to the deep well appearing for the three lowest adiabatic states of the $C_2 + S$ reaction, and the large masses of the three atoms involved, this system has a high density of resonances near the thresholds. Therefore, this reaction is expected to be governed by a statistical mechanism. In this work, we use the adiabatic statistical (AS) method (Quack & Troe 1974), using the recently implemented (Gómez-Carrasco et al. 2022) AZTICC code. Here, we use the rigid rotor approach, which is similar to the method used to treat several reactions and inelastic processes (Konings et al. 2021). We consider the experimental exoergic values of $D_0 = D_0^{C_2} - D_0^{CS} = 1.14$ eV (Huber & Herzberg 1979), which already includes the vibrational zero-point energy (ZPE) of reactants and products. This exothermicity is very close to that shown in the ab initio calculations in Fig. 8, namely of ≈ 1 eV, which does not include ZPE.
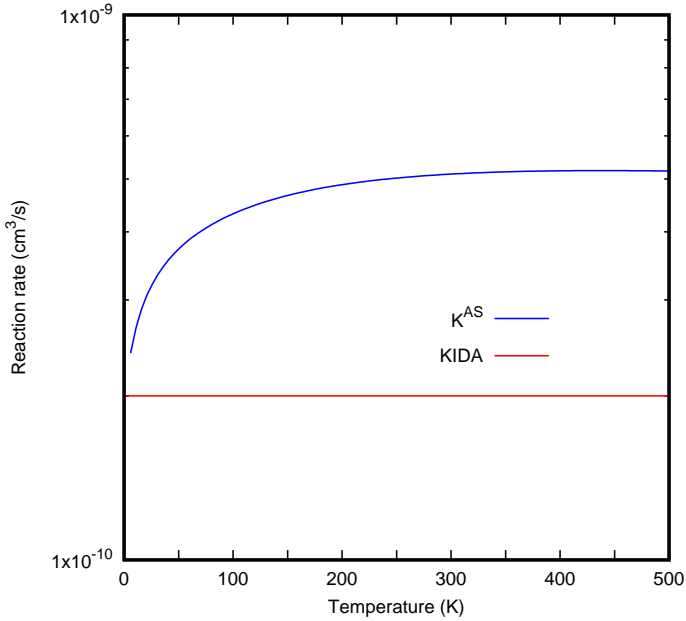
Fig. 9. Reactive rate constant for the $C_2 + S \rightarrow CS + S$ collisions obtained with the present AS method and compared to that available in the KIDA database from Vidal et al. (2017).

In the rigid rotor approach, the diatomic distances for the diatomic molecules are frozen to their equilibrium values, namely r_e = 1.2425 and 1.568 Å for C_2 and CS, respectively. As C_2 is homonuclear, the even and odd rotational channels are not coupled, and are treated independently. The large exothermicity requires the inclusion of vibrational levels for the CS products of up to v = 15 in order to adequately describe the density of states of the products. To this end, the adiabatic potentials are generated for each final v independently using the rigid rotor approximation at r_{eq} with the same long-range potential but shifting the energy using the anharmonic vibration constants, ω_e = 0.15933 eV $\omega_e\chi_e$ = 0.801 meV from Herzberg (1950).

All product ro-vibrational levels are then considered to obtain the square of the S-matrix at each total angular momentum J (see Gómez-Carrasco et al. 2022 for more details). The calculations are done using a body-fixed frame, in which the z-axis is parallel to the Jacobi vector **R**, joining the diatomic center of mass to the atom, and the three atoms are considered in the body-fixed xz-plane. In the present calculations, a maximum rotational quantum numbers of j_{max} = 200 and 250 are considered for C_2 and CS, respectively, together with a maximum helicity quantum number of Ω_{max} = 15. The individual state-to-state reactive cross sections are obtained by performing the summation over all J in the partial wave expression up to J_{max} = 200.

Finally, integrating over the translational energy according to a Boltzmann energy distribution, and summing over all accessible states, the thermal rate constants, $K_\alpha(T)$, are obtained, with $\alpha = 1^3A''$, $1^3A'$, and $1^3A'$. The $2^3A''$ and $1^3A'$ states present a submerged barrier, which could reduce the reactivity; however, here we consider that the three α electronic states have the same reactive rate constant. For this reason, when the spin–orbit splitting of $S(^3P_J)$ is included, the final thermal rate constant averaging over the spin-orbit states, $K^{AS}(T)$, is equal to $K_\alpha(T)$, as shown in Fig. 9; the rate constants have been fit to a modified Arrhenius expression and the parameters obtained are listed in Table 2.

The $C_2 + S \rightarrow CS + S$ available in the KIDA data base[2] is that of Vidal et al. (2017), and corresponds to a value of $K^C(T)$ = 2 10^{-10} cm^3 s^{-1}, which is independent of temperature, and was calculated using a capture method, that is, assuming that the reaction is exothermic, but without considering the deep well described in this work. Such an approach neglects the possibility that the C_2S complex formed under the statistical assumption can exit back to $C_2 + S$ products. This probability is small because it is proportional to the density of states in each channel, and this density is much lower in the $C_2 + S$ due to the exothermicity, the homonuclear symmetry, and the larger rotational constant.

4. Discussion

In this section, we evaluate the impact of the new reaction rates on our understanding of interstellar chemistry. This is not straightforward, because the formation and destruction routes of the different species depend on local physical and chemical conditions, as well as the chemical time. We therefore need to consider different environments in order to obtain a comprehensive view of the impact of the new reactions rates on astrochemical calculations, and in particular on our ability to reproduce the abundance of CS.

We performed chemical calculations using Nautilus 1.1 (Ruaud et al. 2016), a three-phase model in which gas, grain surface, and grain mantle phases, and their interactions, are considered. We used the code upgraded as described by Wakelam et al. (2021), with the chemical network of KIDA[2], which has been modified to account for the reaction rates estimated by Fuente et al. (2016, 2019), and this paper (reaction rates in Table 2). In Nautilus, desorption into the gas phase is only allowed for the surface species, considering both thermal and nonthermal mechanisms. In the regions where the temperature of grain particles is below the sublimation temperature, nonthermal desorption processes become important when calculating the number of molecules in gas phase. The latter includes desorption induced by cosmic rays (Hasegawa & Herbst 1993), direct (UV field), and indirect (secondary UV field induced by the cosmic-ray flux) photo-desorption, and reactive chemical desorption (Garrod et al. 2007; Minissale et al. 2016). In the following calculations, we use the prescription proposed by Minissale et al. (2016) for ice-coated grains to calculate the reactive chemical desorption. The physical and chemical conditions associated with these three simulations are detailed below:

– TMC 1: This case represents the physical and chemical conditions prevailing in molecular cloud complexes where low-mass stars are formed. The physical properties of these regions are typically described with moderate number densities of atomic hydrogen nuclei n_H = 3×10^4 cm^{-3}, cold gas and dust temperatures T = 10 K, a moderate visual extinction A_V = 20 mag, a cosmic-ray H_2 ionization rate of ζ_{H_2} = 10^{-16} s^{-1} (Fuente et al. 2019, 2023), and an intensity of the far-ultraviolet (FUV) field equal to χ = 5 in Draine units. We assume that sulphur is depleted by a factor of 20 relative to the cosmic abundance as derived by Fuente et al. (2019, 2023) in Taurus and Perseus.

– Hot core: This case represents the physical and chemical conditions in the warm interior of young protostars where the gas and dust temperature is >100 K and the icy grain mantles are sublimated. Typical physical conditions in these regions are: n_H = 3×10^6 cm^{-3}, T_k = 200 K, A_V = 20 mag, ζ_{H_2} = 1.3×10^{-17} s^{-1}, and χ = 1 in Draine units. Sulphur depletion in

Table 3. Model predictions using the old and new reaction rate coefficients.

Molecule	Age (Myr)	TMC1-old	TMC1-new	HC-old	HC-new	PDR-old	PDR-new
CS	0.1	1.92×10^{-8}	1.61×10^{-8}	6.33×10^{-11}	6.13×10^{-11}	2.69×10^{-9}	2.88×10^{-9}
	1.0	6.47×10^{-8}	6.47×10^{-8}	2.04×10^{-12}	1.66×10^{-12}	2.89×10^{-9}	3.06×10^{-9}
SO	0.1	1.08×10^{-7}	4.70×10^{-8}	6.36×10^{-7}	6.28×10^{-7}	1.70×10^{-9}	1.70×10^{-9}
	1.0	1.70×10^{-9}	1.67×10^{-9}	4.28×10^{-7}	3.50×10^{-7}	1.82×10^{-9}	1.82×10^{-9}
SO_2	0.1	7.68×10^{-9}	1.41×10^{-8}	1.32×10^{-7}	1.56×10^{-7}	9.99×10^{-14}	1.33×10^{-13}
	1.0	4.28×10^{-11}	2.20×10^{-10}	3.71×10^{-7}	4.49×10^{-7}	1.06×10^{-13}	1.43×10^{-13}

hot cores is not well established. We adopted [S/H]=8×10^{-7} because this value is commonly used to model massive hot cores (Gerner et al. 2014).

– Photon-dominated regions (PDRs) are those environments where the FUV photons emitted by hot stars determin the physical and chemical conditions of gas and dust. PDRs can be found on the surfaces of protoplanetary disks and molecular clouds, globules, planetary nebulae, and starburst galaxies. As representative of the physical and chemical conditions in the PDRs associated with massive star forming regions, we select: $n_H = 5 \times 10^5$ cm^{-3}, $T_k = 100$ K, $A_V = 4$ mag, $\zeta_{H_2} = 10^{-16}$ s^{-1}, and $\chi = 10^4$ in Draine units. The amount of sulphur in gas phase in PDRs is still an open question. Based on observations of sulphur recombination lines in the Orion Bar, Goicoechea & Cuadrado (2021) obtained that the abundance of sulphur should be close to the solar value in this prototypical PDR. We are aware that sulphur recombination lines arise from PDR layers close to the S$^+$/S transition, at $A_v \sim 4$ mag (Simon et al. 1997; Goicoechea et al. 2006) and sulphur depletion might be higher toward more shielded regions from where the emission of most sulphur-bearing molecules comes. In spite of this, we adopt [S/H]=1.5×10^{-5} for our calculations.

Table 3 shows the fractional abundances of CS, SO, and SO_2 predicted using the "old" and "new" chemical network and the physical conditions described above. In regions where the ionization fraction is large, CS is essentially produced from the electronic dissociative recombination of HCS$^+$, where HCS$^+$ is formed by reactions of S$^+$ and CH (Sternberg & Dalgarno 1995; Lucas & Liszt 2002). Vidal et al. (2017) showed that the production of HCS$^+$ with S$^+$ + CH → CS$^+$ + H and CS$^+$ + H$_2$ → HCS$^+$ + H is the most efficient HCS$^+$ formation route at the cloud surface. In more shielded regions, where the sulphur is mainly in neutral atomic form, CS is also produced by neutral-neutral reactions, with significant contributions of the reactions studied in this paper. For dark cloud conditions, the reaction C$_2$ + S forms CS more efficiently than CH + S. At low temperatures, the calculated C$_2$ + S rate is slightly higher than previous values (see Fig. 9). However, its possible effect is canceled by the lower value of the new CH + S reaction rate (see Fig. 6). As a result, the impact of our new rates on the CS abundance for the TMC1 case is negligible. Unsurprisingly, the major impact of the new reaction rates calculated on the CS abundance is observed for the hot core case with variations of about 20% due to the significantly higher C$_2$ + S reaction rate at temperatures >100 K (see Fig. 9). The S + O$_2$ → SO + O and SO + OH → SO$_2$ + H reactions rates published by Fuente et al. (2016, 2019) produce the maximum variations in the case TMC1, with variations of the SO and SO$_2$ abundances of a factor of >2, which demonstrates the need to perform this type of calculation.

TMC 1 (CP) is the astrophysical object for which the highest number of sulphur-bearing species have been detected so far, with more than ten complex sulphur-bearing molecules detected for the first time in the last 3 yr (Cernicharo et al. 2021b; Fuentetaja et al. 2022, Table 4). The large number of atoms in these new species (>5) shows that a rich and complex organo-sulphur chemistry is going on in this dark cloud (Laas & Caselli 2019). Although these large molecules carry a small percentage of the sulphur budget, their detection is useful for testing the predictive power of our chemical network. Table 4 shows a compilation of the observed abundances toward TMC 1 (CP). In order to perform the most uniform and reliable comparison, we recalculated the abundances assuming N$_H$ = 3.6×10^{22} cm^{-2} (Fuente et al. 2019). The abundances of HCS$^+$ and H^{13}CN were estimated by Rodríguez-Baras et al. (2021); here, we recalculated them using the most recent collisional coefficients reported by Denis-Alpizar et al. (2022) and Navarro-Almaida et al. (2023). Following the same methodology explained in Fuente et al. (2019) and Rodríguez-Baras et al. (2021), we assumed X(HCN)/X(H^{13}CN) = 60 to estimate the HCN abundance.

We performed chemical calculations using Nautilus 1.1 and the chemical network modified to account for the reaction rates presented in this paper, Fuente et al. (2016, 2019), and the physical conditions derived by Fuente et al. (2023). These physical conditions are the same as in the TMC1 case in Table 3. Only 17 of the total number of sulphur-bearing species detected toward TMC 1 (CP) are included in our chemical network. Figure 10 shows the chemical predictions for all the sulphur-bearing species observed in this proto-typical source and included in our chemical network. In addition, we show the CO, HCO$^+$, and HCN abundances because these molecules are considered good tracers of the gas ionization degree and C/O ratio (Fuente et al. 2019).

We find reasonable agreement (within a factor of 10) between model and observations for CO, HCO$^+$, HCN, CS, HCS$^+$, H$_2$S, SO, C$_2$S, C$_3$S, C$_4$S, H$_2$CS, HC$_2$S$^+$, HC$_3$S$^+$, H$_2$CCS, NS$^+$, HNCS, and HSCN for times between 0.1 Myr and 1 Myr. However, as mentioned by Bulut et al. (2021) and Wakelam et al. (2021), the chemical time at which we find the best solutions depends on the considered species. The most important restrictions with respect to the chemical time comes for CO and HCO$^+$, whose abundances rapidly decrease for times later than 0.4 Myr. On the contrary, we find that the abundances of HCS$^+$, SO, and C$_2$S are better reproduced for times >1 Myr. Only OCS, C$_4$S, and NS cannot be fitted with chemical times between 0.1 Myr and 1 Myr. We would like to reiterate that the chemical time is not the same as the dynamical time, as various physical phenomena – such as turbulent motions that carry molecules to the cloud surfaces, or shocks – can reset the chemical age of the gas. Sulphur-bearing species are very sensitive to the chemical time, and there are several species whose abundances vary by several

Table 4. Chemical abundances in TMC 1 (CP).

Species	Observed		Model (0.1 Myr)	Model (1 Myr)
H_2	0.5			
CS	$6.5 \times 10^{-9(1)}$	$6.4 \times 10^{-9(2)}$	1.6×10^{-8}	6.5×10^{-8}
CO	$4.8 \times 10^{-5(1)}$	$4.2 \times 10^{-5(2)}$	1.0×10^{-4}	6.8×10^{-6}
HCO^+	$5.0 \times 10^{-9(1)}$	$8.4 \times 10^{-9(2)}$	1.0×10^{-8}	2.0×10^{-9}
HCS^+	$1.1 \times 10^{-10(*)}$	$7.0 \times 10^{-11(1)}$	2.3×10^{-11}	1.4×10^{-10}
HCN	$4.8 \times 10^{-8(*)}$	$3.5 \times 10^{-8(2)}$	5.0×10^{-8}	2.1×10^{-7}
SO	$9.0 \times 10^{-10(1)}$	$5.3 \times 10^{-10(2)}$	4.7×10^{-8}	1.7×10^{-9}
OCS	$1.2 \times 10^{-10(2)}$		3.2×10^{-9}	4.5×10^{-9}
H_2S	$8.0 \times 10^{-10(2)}$	$1.1 \times 10^{-9(3)}$	1.4×10^{-9}	1.3×10^{-8}
H_2CS	$1.1 \times 10^{-9(4)}$		2.1×10^{-9}	6.7×10^{-8}
C_2S	$2.8 \times 10^{-9(4)}$		2.6×10^{-10}	9.4×10^{-9}
C_3S	$3.8 \times 10^{-10(4)}$		3.9×10^{-10}	3.3×10^{-9}
HCSCN	$8.9 \times 10^{-12(5)}$			
HCSCCH	$2.2 \times 10^{-12(5)}$			
NCS	$2.2 \times 10^{-11(5)}$			
HCCS	$1.9 \times 10^{-11(5)}$		1.0×10^{-11}	1.1×10^{-8}
H_2CCS	$2.2 \times 10^{-11(5)}$		2.1×10^{-11}	4.7×10^{-11}
H_2CCCS	$1.0 \times 10^{-11(5)}$			
C_4S	$1.0 \times 10^{-12(5)}$		6.2×10^{-12}	3.1×10^{-10}
C_5S	$1.4 \times 10^{-12(5)}$			
HC_3S^+	$5.5 \times 10^{-12(5)}$		9.3×10^{-12}	6.5×10^{-11}
HSCN	$1.9 \times 10^{-12(6)}$		6.3×10^{-13}	1.3×10^{-10}
HNCS	$1.9 \times 10^{-12(6)}$		8.8×10^{-13}	2.0×10^{-10}
HCCCCS	$2.6 \times 10^{-12(7)}$			
$HCCS^+$	$3.0 \times 10^{-11(8)}$		1.4×10^{-11}	1.3×10^{-10}
NS^+	$1.4 \times 10^{-12(9)}$		1.7×10^{-11}	1.5×10^{-12}
NS	$4.7 \times 10^{-11(9)}$		2.2×10^{-10}	1.0×10^{-9}
HCS	$1.5 \times 10^{-10(5)}$		2.1×10^{-11}	3.1×10^{-10}

References. (1) Fuente et al. (2019), (2) Rodríguez-Baras et al. (2021), (3) Navarro-Almaida et al. (2020), (4) Gratier et al. (2016), (5) Cernicharo et al. (2021b), (6) Adande et al. (2010), (7) Fuentetaja et al. (2022), (8) Cernicharo et al. (2021a), (9) Cernicharo et al. (2018), (*) Calculated in this work.

orders of magnitude from 0.1 Myr to 1 Myr. Therefore, the chemical time is a critical parameter in fitting them (see Fig.10). In our 0D chemical calculations, the physical conditions remain fixed, which is far from the real case of a collapsing and fragmenting cloud. In forthcoming papers, we will explore the influence that the cloud dynamical evolution can have on the sulphur chemistry.

5. Summary and conclusions

In this work, we obtained the rate constants for the formation of $CS(X^1\Sigma^+)$, $CH(^2\Pi) + S(^3P)$, and $C_2(X^1\Sigma_g^+) + S(^3P)$; these are listed in Table 2. These two reactions involve open shell reactants and therefore present several degenerate or nearly degenerate electronic states. We analyzed the role of each initial electronic state in the formation of CS in detail.

For $CH(^2\Pi) + S(^3P)$, we find that only the $1^2A'$ can contribute to $CS(X^1\Sigma^+)$ formation through an exothermic barrierless mechanism, that is, 2 states of the doublet among the 36 degenerate electronic states correlating to the $CH(^2\Pi) + S(^3P)$ asymptote. When the spin-orbit splitting is taken into account, at the low temperatures of 10 K, the electronic partition function becomes 2/9, tending to 2/36 at high temperature. Surprisingly, the rate constant obtained with a capture model (Vidal et al. 2017) is only a factor of two higher than the present result at

10 K, and this difference increases very little with increasing temperature up to 500 K.

For the $C_2(X^1\Sigma_g^+) + S(^3P)$ reaction, the three triply degenerate states connect to the $CS(X^1\Sigma^+)$ products. We find that three states present a deep insertion well, with depths of between 5.5 and 4 eV. The ground electronic state proceeds with no barrier, while the two excited states have a barrier in the product channel, which becomes submerged in a bent configuration. The presence of the deep insertion well justifies the use of an adiabatic statistical method to calculate the reactive rate constant, which in turn is very similar to that obtained with a capture model (Vidal et al. 2017) at 10 K. The difference increases with temperature, and the present results become 2.5 times larger than the constant value obtained 2×10^{-10} cm^3 s^{-1} at 500 K.

The present results corroborate those obtained with classical capture models at low temperatures, differing by a factor of 2.5 at most. However, it should be noted that this is due to different factors for the two reactions studied here. For open shell reactants, such as those treated here, for which experiments are difficult, a detailed analysis of the reactivity of all initial degenerate electronic states of the reactants is required before generalizing these findings.

The new rates have been implemented in a chemical network to compare with the observations of sulphur-bearing species
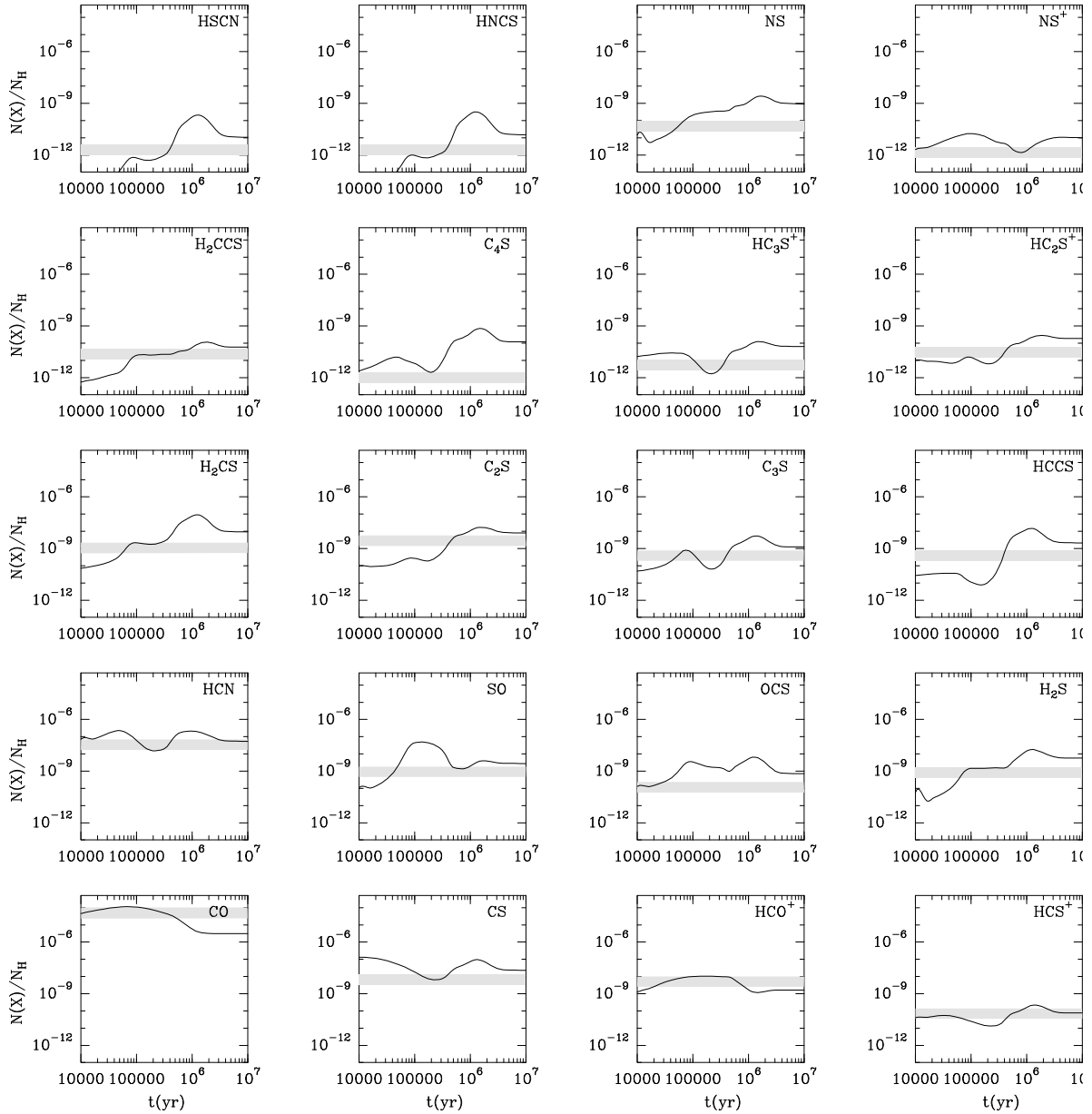
Fig. 10. Comparison between Nautilus predictions obtained using our updated chemical network and the abundances observed toward TMC 1 (CP; see Table 4). Gray regions indicate the observed values. We assume an uncertainty of a factor of 2 in the measured abundances. The physical and chemical conditions used in our calculations are: $n_H = 3 \times 10^4$ cm^{-3}, $T_k = 10$ K, $A_V = 20$ mag, $\zeta_{H_2} = 10^{-16}$ s^{-1}, $G_0=1$ in Draine units and [S/H] = 7.5×10^{-7} (sulphur depleted by a factor of ~20).

toward TMC 1(CP). Model predictions are in reasonable agreement with observations for most of the sulphur-bearing species, except for OCS and NS, which cannot be fitted with our model. However, it is not possible to fit all of them with a unique chemical time, which suggests that dynamical effects are important for sulphur chemistry.

References

Adande, G. R., Halfen, D. T., Ziurys, L. M., Quan, D., & Herbst, E. 2010, ApJ, 725, 561
Aguado, A., & Paniagua, M. 1992, J. Chem. Phys., 96, 1265
Aguado, A., Tablero, C., & Paniagua, M. 1998, Comput. Phys. Commun., 108, 259
Agúndez, M., & Wakelam, V. 2013, Chem. Rev., 113, 8710
Alexander, M. H. 1998, J. Chem. Phys., 108, 4467
Atahan, S., Kłos, J., Zuchowski, P. S., & Alexander, M. H. 2006, Phys. Chem. Chem. Phys., 8, 4420
Boogert, A. C. A., Schutte, W. A., Helmich, F. P., Tielens, A. G. G. M., & Wooden, D. H. 1997, A&A, 317, 929

Bulut, N., Roncero, O., Aguado, A., et al. 2021, A&A, 646, A5
Cazaux, S., Carrascosa, H., Muñoz Caro, G. M., et al. 2022, A&A, 657, A100
Cernicharo, J., Lefloch, B., Agúndez, M., et al. 2018, ApJ, 853, L22
Cernicharo, J., Cabezas, C., Endo, Y., et al. 2021a, A&A, 646, A3
Cernicharo, J., Cabezas, C., Endo, Y., et al. 2021b, A&A, 650, A14
Davidson, E. R. 1975, J. Comp. Phys., 17, 87
Denis-Alpizar, O., Quintas-Sánchez, E., & Dawes, R. 2022, MNRAS, 512, 5546
Dubernet, M. L., & Hutson, J. 1994, J. Chem. Phys., 101, 1939
Dunning, T. H., Jr. 1989, J. Chem. Phys., 90, 1007
Esplugues, G., Fuente, A., Navarro-Almaida, D., et al. 2022, A&A, 662, A52
Ferrante, R. F., Moore, M. H., Spiliotis, M. M., & Hudson, R. L. 2008, ApJ, 684, 1210
Flower, D. R., & Launay, J. M. 1977, J. Phys. B: At. Mol. Phys., 10, 3673
Fuente, A., Cernicharo, J., Roueff, E., et al. 2016, A&A, 593, A94
Fuente, A., Navarro, D. G., Caselli, P., et al. 2019, A&A, 624, A105
Fuente, A., Rivière-Marichalar, P., Beitia-Antero, L., et al. 2023, A&A, 670, A114
Fuentetaja, R., Agúndez, M., Cabezas, C., et al. 2022, A&A, 667, A4
Garrod, R. T., Wakelam, V., & Herbst, E. 2007, A&A, 467, 1103
Georgievskii, Y., & Klippenstein, S. J. 2005, J. Chem. Phys., 122, 194103
Gerner, T., Beuther, H., Semenov, D., et al. 2014, A&A, 563, A97
Goicoechea, J. R., & Cuadrado, S. 2021, A&A, 647, A7
Goicoechea, J. R., Pety, J., Gerin, M., et al. 2006, A&A, 456, 565
Goicoechea, J. R., Aguado, A., Cuadrado, S., et al. 2021, A&A, 647, A10
Gómez-Carrasco, S., Félix-González, D., Aguado, A., & Roncero, O. 2022, J. Chem. Phys., 157, 084301
Gratier, P., Majumdar, L., Ohishi, M., et al. 2016, ApJS, 225, 25
Grozdanov, T. P., & Solov'ev, E. A. 1982, J. Phys. B, 15, 1195
Gu, X., Guo, Y., Zhang, F., Mebel, A. M., & Kaiser, R. I. 2006, Faraday Discuss., 133, 245
Hapka, M., Żuchowski, P. S., Szczęśniak, M. M., & Chałasiński, G. 2012, J. Chem. Phys., 137, 164104
Hasegawa, T. I., & Herbst, E. 1993, MNRAS, 261, 83
Herzberg, G. 1950, Molecular Spectra and Molecular Structure. I. Spectra of Diatomic Molecules (New Yok: van Nostrand Reinhold Co.)
Hily-Blant, P., des Forêts, G. P., Faure, A., & Lique, F. 2022, A&A, 658, A168
Huber, K. P., & Herzberg, G. 1979, Molecular Spectra and Molecular Structure, IV. Constants of Diatomic Molecules (Toronto: Van Nostrand)
Jiménez-Escobar, A., & Muñoz Caro, G. M. 2011, A&A, 536, A91
Jiménez-Escobar, A., Muñoz Caro, G. M., & Chen, Y. J. 2014, MNRAS, 443, 343
Karplus, M., Porter, R. N., & Sharma, R. D. 1965, J. Chem. Phys., 43, 3259
Kendall, R. A., Dunning, T. H., & Harrison, R. J. 1992, J. Chem. Phys., 96, 6796
Klos, J., Szczesniak, M. M., & Chalasinski, G. 2004, Int. Rev. Phys. Chem., 23, 541
Konings, M., Desrousseaux, B., Lique, F., & Loreau, J. 2021, J. Chem. Phys., 155, 104302
Laas, J. C., & Caselli, P. 2019, A&A, 624, A108
Lucas, R., & Liszt, H. S. 2002, A&A, 384, 1054
McClure, M. K., Rocha, W. R. M., Pontoppidan, K. M., et al. 2023, Nat. Astron., 7, 431
Minissale, M., Dulieu, F., Cazaux, S., & Hocuk, S. 2016, A&A, 585, A24

Nagy, T., & Lendvay, G. 2017, J. Phys. Chem. Lett., 8, 4621
Navarro-Almaida, D., Le Gal, R., Fuente, A., et al. 2020, A&A, 637, A39
Navarro-Almaida, D., Bop, C. T., Lique, F., et al. 2023, A&A, 670, A110
Ocaña, A. J., Jiménez, E., Ballesteros, B., et al. 2017, ApJ, 850, 28
Palumbo, M. E., Tielens, A. G. G. M., & Tokunaga, A. T. 1995, ApJ, 449, 674
Palumbo, M. E., Geballe, T. R., & Tielens, A. G. G. M. 1997, ApJ, 479, 839
Páramo, A., Canosa, A., Le Picard, S. D., & Sims, I. R. 2008, J. Phys. Chem. A, 112, 9591
Qu, C., & Bowman, J. M. 2016, J. Phys. Chem. A, 120, 4988
Quack, M., & Troe, J. 1974, Ber. Bunsenges. Phys. Chem, 78, 240
Reddy, R. R., Nazeer Ahammed, Y., Rama Gopal, K., & Baba Basha, D. 2003, Astrophys. Space Sci., 286, 419
Riaplov, E., Wyss, M., Maier, J. P., et al. 2003, J. Mol. Spectrosc., 222, 15
Rivière-Marichalar, P., Fuente, A., Goicoechea, J. R., et al. 2019, A&A, 628, A16
Rodríguez-Baras, M., Fuente, A., Rivière-Marichalar, P., et al. 2021, A&A, 648, A120
Roncero, O., Zanchet, A., & Aguado, A. 2018, Phys. Chem. Chem. Phys., 20, 25951
Ruaud, M., Wakelam, V., & Hersant, F. 2016, MNRAS, 459, 3756
Saito, S., Kawaguchi, K., Yamamoto, S., et al. 1987, ApJ, 317, L115
Sanz-Sanz, C., Aguado, A., Roncero, O., & Naumkin, F. 2015, J. Chem. Phys., 143, 234303
Senekowitsch, J., Carter, S., Rosmus, P., & Werner, H.-J. 1990, Chem. Phys., 147, 281
Shingledecker, C. N., Lambers, T., Laas, J. C., et al. 2020, ApJ, 888, 52
Simon, R., Stutzki, J., Sternberg, A., & Winnewisser, G. 1997, A&A, 327, L9
Song, Y.-Z., Zhang, L.-L., Gao, S.-B., & Meng, Q.-T. 2016, Scientific Rep., 6, 37734
Spezzano, S., Fuente, A., Caselli, P., et al. 2022, A&A, 657, A10
Sternberg, A., & Dalgarno, A. 1995, ApJS, 99, 565
Stoecklin, T., Halvick, P., & Rayez, J. C. 1988, J. Mol. Struct. (Theochem), 163, 267
Stoecklin, T., Rayez, J. C., & Duguay, B. 1990a, Chem. Phys., 148, 381
Stoecklin, T., Rayez, J. C., & Duguay, B. 1990b, Chem. Phys., 148, 399
Tarroni, R., Carter, S., & Handy, N. C. 2007, Mol. Phys., 105, 1129
Vastel, C., Quénard, D., Le Gal, R., et al. 2018, MNRAS, 478, 5514
Vidal, T. H. G., Loison, J.-C., Jaziri, A. Y., et al. 2017, MNRAS, 469, 435
Visser, B., Beck, M., Bornhauser, P., et al. 2019, Mol. Phys., 117, 1645
Voronin, A. I. 2004, Chem. Phys., 297, 49
Wakelam, V., Dartois, E., Chabot, M., et al. 2021, A&A, 652, A63
Werner, H. J., & Knowles, P. J. 1988a, J. Chem. Phys., 89, 5803
Werner, H. J., & Knowles, P. J. 1988b, Chem. Phys. Lett., 145, 514
Werner, H. J., Knowles, P. J., Knizia, G., Manby, F. R., & Schütz, M. 2012, WIREs Comput. Mol. Sci., 2, 242
Woon, D. E., & Herbst, E. 2009, ApJS, 185, 273
Zanchet, A., Roncero, O., González-Lezana, T., et al. 2009, J. Phys. Chem. A, 113, 14488
Zanchet, A., Roncero, O., & Bulut, N. 2016, Phys. Chem. Chem. Phys., 18, 11391
Zanchet, A., del Mazo, P., Aguado, A., et al. 2018, PCCP, 20, 5415
Zeimen, W. B., Klos, J., Groenenboom, G. C., & van der Avoird, A. 2003, J. Chem. Phys., 118, 7340
Zhang, L. L., Song, Y. Z., Gao, S. B., & Meng, Q. T. 2018, J. Phys. Chem. A, 122, 4390